Research Square

Preprints are preliminary reports that have not undergone peer review.
They should not be considered conclusive, used to inform clinical practice,
or referenced by the media as validated information.

Helicity-Resolved Valley-Selective Second Harmonic Generation in Monolayer MoS2 for Optical Defect Metrology

Chen-Yu Wang
National Cheng Kung University
Yu-Zen Lee
National Cheng Kung University
Tzu-En Huang
National Cheng Kung University
Neng-An Huang
National Cheng Kung University
Ming-Jin Liu
National Tsing Hua University
Jyun-Yu Chen
National Chung Hsing University
Mon-Shu Ho
National Chung Hsing University
Yu-Lun Chueh
National Tsing Hua University
Kuang-Yao Lo
kuanglo@mail.ncku.edu.tw

National Cheng Kung University

Article

Keywords: Valley Polarization, Helicity Photon, Circular Polarization, Second Harmonic Generation, Monolayer MoS2, 2D Material, Defect Characterization

Posted Date: November 16th, 2026

DOI: https://doi.org/10.21203/rs.3.rs-11383864/v1

License: This work is licensed under a Creative Commons Attribution 4.0 International License.
Read Full License

Additional Declarations: No competing interests reported.

Helicity-Resolved Valley-Selective Second Harmonic Generation in Monolayer MoS_2 for Optical Defect Metrology

*Chen-Yu Wang[1], Yu-Zen Lee[1], Tzu-En Huang[1], Neng-An Huang[1], Ming-Jin Liu[2], Jyun-Yu Chen[3], Mon-Shu Ho[3,] * , Yu-Lun Chueh[2, 4, 5,] * , Kuang-Yao Lo[1, 6,] **

[1]Department of Physics, National Cheng Kung University, Tainan 701401, Taiwan

[2]Department of Materials Science and Engineering, National Tsing Hua University, Hsinchu 300044, Taiwan.

[3]Department of Physics, National Chung Hsing University, Taichung 40227, Taiwan

[4]College of Semiconductor Research, National Tsing Hua University, Hsinchu, 30013, Taiwan.

[5]Department of Materials Science and Engineering, Korea University, Seoul 02841, Republic of Korea.

[6]Academy of Innovative Semiconductor and Sustainable Manufacturing, National Cheng Kung University, Tainan 701401, Taiwan

*Correspondence authors: msho@dragon.nchu.edu.tw , ylchueh@mx.nthu.edu.tw , kuanglo@mail.ncku.edu.tw

Abstract

Structural defects critically affect the optical and electronic properties of 2D materials, yet existing characterization methods are often destructive, insufficiently sensitive, or unsuitable for large-area analysis. Here we develop a helicity-resolved second-harmonic generation (HR-SHG) microscopy method that enables quantitative evaluation of defects in monolayer MoS_2 through defect-induced valley depolarization. By separately resolving the two circularly polarized components, rather than relying solely on the total SHG intensity, we extract the degree of polarization as a direct optical indicator of defect-induced valley depolarization. The measured response tracks the structural, optical, chemical, and electronic evolution of plasma-induced defects revealed by complementary characterization and distinguishes subtle defect variations that are not readily resolved by conventional optical techniques. The method is non-destructive, ultrahigh sensitivity, operable at room temperature, compatible with rapid large-area mapping, and potentially suitable for real-time quality monitoring and scalable defect engineering in 2D materials.

Keywords

Valley Polarization, Helicity Photon, Circular Polarization, Second Harmonic Generation, Monolayer MoS_2, 2D Material, Defect Characterization

Introduction

Transition Metal Dichalcogenides (TMDs) as a 2D material have attracted considerable interest for next-generation electronic, optoelectronic and quantum devices owing to their atomically thin structures, tunable band structures and valley-dependent properties.[1-5] However, their optical and electronic responses are highly sensitive to lattice defects, which introduce localized electronic states, alter carrier transport and degrade device performance.[6-11] Reliable characterization and quantitative evaluation of these defects are therefore essential for both fundamental studies and technological applications.[12]

Existing characterization techniques provide complementary information but have distinct limitations. Raman and photoluminescence (PL) spectroscopy probe lattice vibrations and excitonic recombination, respectively, but detect defects only indirectly through spectral shifts, broadening or intensity quenching, limiting their sensitivity to subtle variations in defect density.[13-15] X-ray photoelectron spectroscopy (XPS) identifies sulfur depletion, oxidation and other defect-related chemical states, but typically requires ex situ measurements and offers limited capability for rapid large-area mapping.[16] Kelvin probe force microscopy (KPFM) maps defect-induced changes in surface potential and work function, whereas scanning tunnelling microscopy (STM) provides atomic-scale structural and electronic information but is restricted by demanding operating conditions and small scanning areas.[17] Linearly polarized SHG is sensitive to defect-induced symmetry changes, but does not directly probe the associated valley-dependent electronic evolution.[18,19]

Here we develop a helicity-resolved second-harmonic generation (HR-SHG) microscopy method for quantitative evaluation of plasma-induced defects in monolayer MoS_2. By separately resolving the two circularly polarized (CP) components under valley-selective excitation, we extract the degree of polarization (DOP) as an optical measure of defect-induced valley depolarization. The resulting SHG response is compared with AFM, Raman, PL, XPS, KPFM, STM and linearly polarized SHG measurements, establishing consistent correlations with the structural, optical, chemical and electronic evolution of the defects. This contact-free method operates at room temperature, distinguishes subtle defect variations and enables rapid large-area mapping, providing a scalable optical approach for defect monitoring and engineering in two-dimensional materials.[20,21]

Multi-Characterization of Defects in Monolayer MoS_2

Monolayer MoS_2 samples were exposed to Ar plasma for durations of 0–70 s to introduce progressively increasing defect levels. The AFM image of the pristine sample in figure 1a shows an atomically flat surface with a root-mean-square roughness of 0.129 nm and a thickness of

approximately 0.8 nm, confirming the monolayer morphology and high initial crystalline quality.

Raman spectra acquired with 532 nm excitation are shown in figure 1b. The pristine sample exhibits sharp and intense characteristic vibrational modes. Only minor intensity changes are observed after 15 s of plasma exposure, indicating that the corresponding defect variation remains difficult to resolve by Raman spectroscopy. At 45 s, both modes decrease substantially in intensity, whereas after 70 s they are nearly suppressed, reflecting severe lattice disorder. The PL spectra in figure 1c exhibit a similar trend, with progressive intensity quenching and spectral broadening as the treatment duration increases, consistent with enhanced non-radiative recombination in increasingly defective samples.[22]

XPS was used to examine the chemical evolution of the plasma-induced defects in samples treated for 0, 3 and 15 s, as shown in figure 1d and 1e. After 3 s, the S-2p intensity decreases slightly and the spectral envelope broadens, indicating preferential sulfur removal and the formation of predominantly isolated sulfur vacancies. After 15 s, the S-2p features broaden further and the S/Mo atomic ratio decreases, suggesting that prolonged plasma exposure produces not only a higher defect concentration but also multiple reconstructed and oxidized sulfur-related environments. These results indicate a transition from isolated sulfur vacancies to chemically more complex defect structures. Detailed peak fitting, chemical-state assignments and compositional analysis are provided in Supplementary Information S.1.

KPFM measurements provide a consistent electronic signature of this evolution, as detailed in Supplementary Information S.2. The work function decreases from 4.82 eV in the pristine sample to 4.67 eV after 3 s, and then partially recovers to 4.73 eV after 15 s. This non-monotonic change is consistent with the initial formation of sulfur-vacancy-related donor states followed by defect reconstruction and oxidation.

Finally, linearly polarized SHG measurements were performed under parallel-polarized (SS) and perpendicular-polarized (SP) detection configurations, as shown in figure 1f and 1g. In both configurations, the SHG intensity increases systematically with plasma-treatment duration, demonstrating that the nonlinear optical response is sensitive to defect accumulation. The results directly reveal an increase in the effective second-order hyperpolarizability with increasing plasma-treatment duration.[19,23] However, the aforementioned approach lacks a physical correlation between defect-induced electronic states and the evolution of the band structure—a limitation that is particularly significant for monolayer TMDs, which are characterized by valley polarization in their band structure.

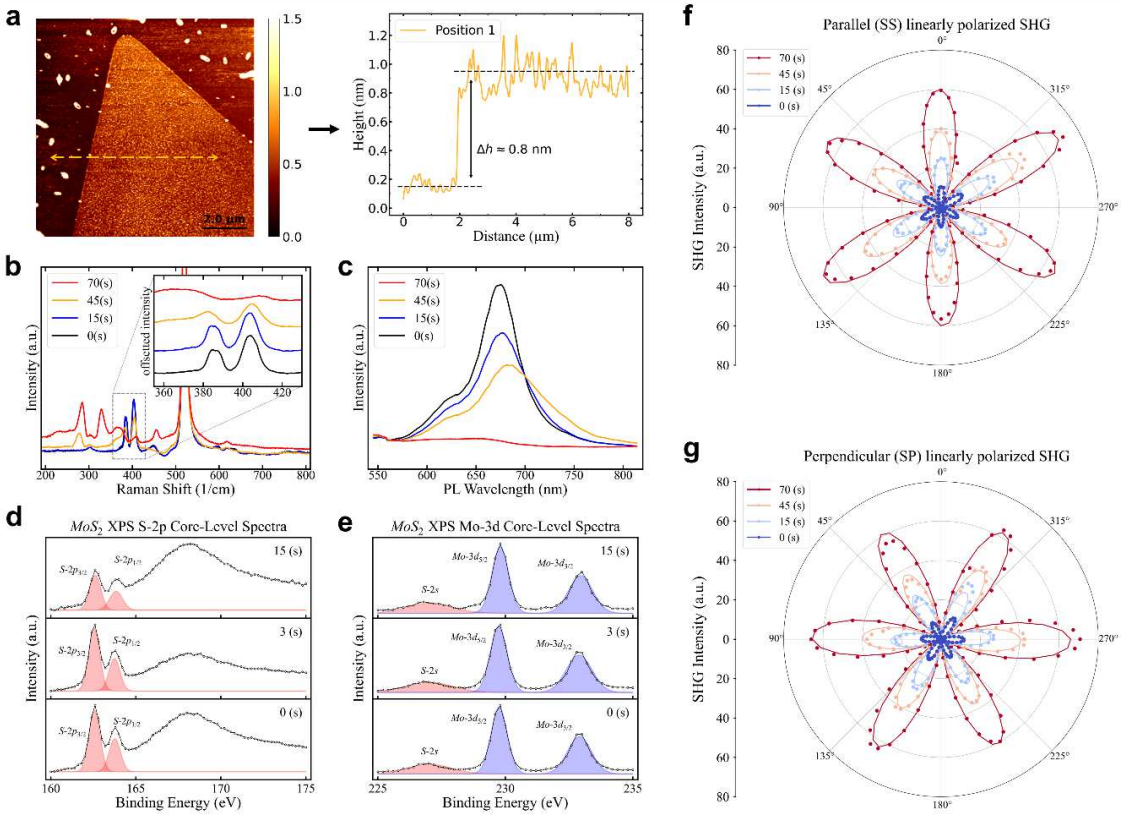


Figure 1. Structural, spectroscopic, chemical, and nonlinear optical characterization of monolayer MoS_2 with controlled defect densities. a, Representative AFM image of an as-grown monolayer MoS_2 sample, showing a smooth and uniform surface. **b,** Raman and **c,** PL spectra of MoS_2 samples subjected to Ar plasma treatment for 0, 15, 45, and 70 s. With increasing plasma-treatment duration, the Raman and PL peaks progressively broaden and decrease in intensity, indicating increasing structural disorder and defect density. **d,** S-2p and **e,** Mo-3d XPS spectra of monolayer MoS_2 subjected to Ar plasma treatment for 0, 3, and 15 s. The progressive evolution of the spectral components indicates plasma-induced chemical disorder and the formation of defect-related chemical states. **f,** Parallel-polarized (SS) and **g,** perpendicular-polarized (SP) azimuthal SHG responses of MoS_2 samples subjected to 0, 15, 45 and 70 s Ar plasma-treatment durations, showing the increase of the SHG intensity and effective second-order hyperpolarizability with increasing defect density.

Defect-Induced Valley Depolarization in MoS_2

Monolayer MoS_2 exhibits a direct bandgap at the inequivalent K and K' points. In this structure, the excitonic band structure shows a valley-selective correspondence with the helicity of incident CP light (σ^+ and σ^-). Specifically, σ^+ photon exclusively excites A excitons at the K point,

while σ^- addresses those at the K' point. This valley-selective excitation arises from the orbital angular momentum characteristics of the energy bands, predominantly originating from Mo d-orbitals and the strong spin-orbit coupling (SOC) that leads to a spin-split valence band at K and K', each corresponding to a distinct photon helicity.[24,25] This valley-selective excitation is a direct consequence of the angular momentum character of the involved electronic states and the underlying symmetry of the material. Faiha Mujeeb et al. demonstrate that CP light can selectively and efficiently generate excitons in a specific valley. When resonantly exciting the A exciton, the observation exhibited nearly perfect helicity. In an ideal case, excitons generated at the K valley via σ^+ excitation will recombine radiatively within the same valley, emitting polarized light. However, intervalley scattering or defect-induced trapping can result in exciton transfer to the K' valley or to defect states, thereby reducing the observed polarization degree.[26]

The same valley-selective symmetry is retained in the HR-SHG response. Under CP excitation, the two SHG components reflect the imbalance between the valley populations, such that their intensity contrast provides an optical measure of valley polarization.[27-29] The detailed electronic Hamiltonian, optical selection rules and second-order susceptibility are provided in Supplementary Information S.3. Structural defects are therefore expected to reduce the helicity contrast by introducing electronic states and additional scattering pathways that relax the intrinsic valley-selective selection rules. To identify the electronic origin of this depolarization, we performed first-principles calculations of pristine and S-vacancy-containing monolayer MoS_2 and compared the calculated electronic structures with STM differential-conductance measurements.[26,30-32]

First-principles calculations were performed using a 4×4 monolayer MoS_2 supercell containing a single S vacancy, with SOC included throughout the structural relaxation and electronic-structure calculations; full computational details are provided in Methods. The calculated band structures reveal that structural defects introduce localized electronic states within the bandgap, as shown in figure 2a, in good agreement with previous first-principles calculations of defect-induced electronic states in MoS_2.[9,33-37] These defect-induced states provide additional angular momentum compensation channels beyond the intrinsic threefold lattice symmetry, thereby relaxing the valley-selective optical selection rules and facilitating defect-assisted intervalley population transfer.

As schematically illustrated in figure 2b, the presence of mid-gap defect states also enables resonant intermediate states in the SHG process, which not only enhances the overall SHG efficiency but simultaneously promotes valley depolarization during nonlinear emission. In figure 2c, the STM-derived differential conductance spectra further support the formation of defect-associated electronic states after Ar plasma treatment. With increasing plasma exposure time, the spectral features gradually evolve, indicating a modification of the local electronic structure in monolayer MoS_2. Notably, after 15 s of plasma treatment, the much higher concentration of sulfur vacancies, edge sulfur, amorphous sulfur, and oxidized sulfur species generates a significantly

larger density of defect-induced electronic states. Consequently, pronounced defect-related states emerge, leading to further band-gap narrowing and enhanced local density of states near the Fermi level. These defect states can provide additional scattering channels and resonant intermediate pathways, consistent with the enhanced SHG intensity and reduced valley-selective response observed in the defect-rich samples.

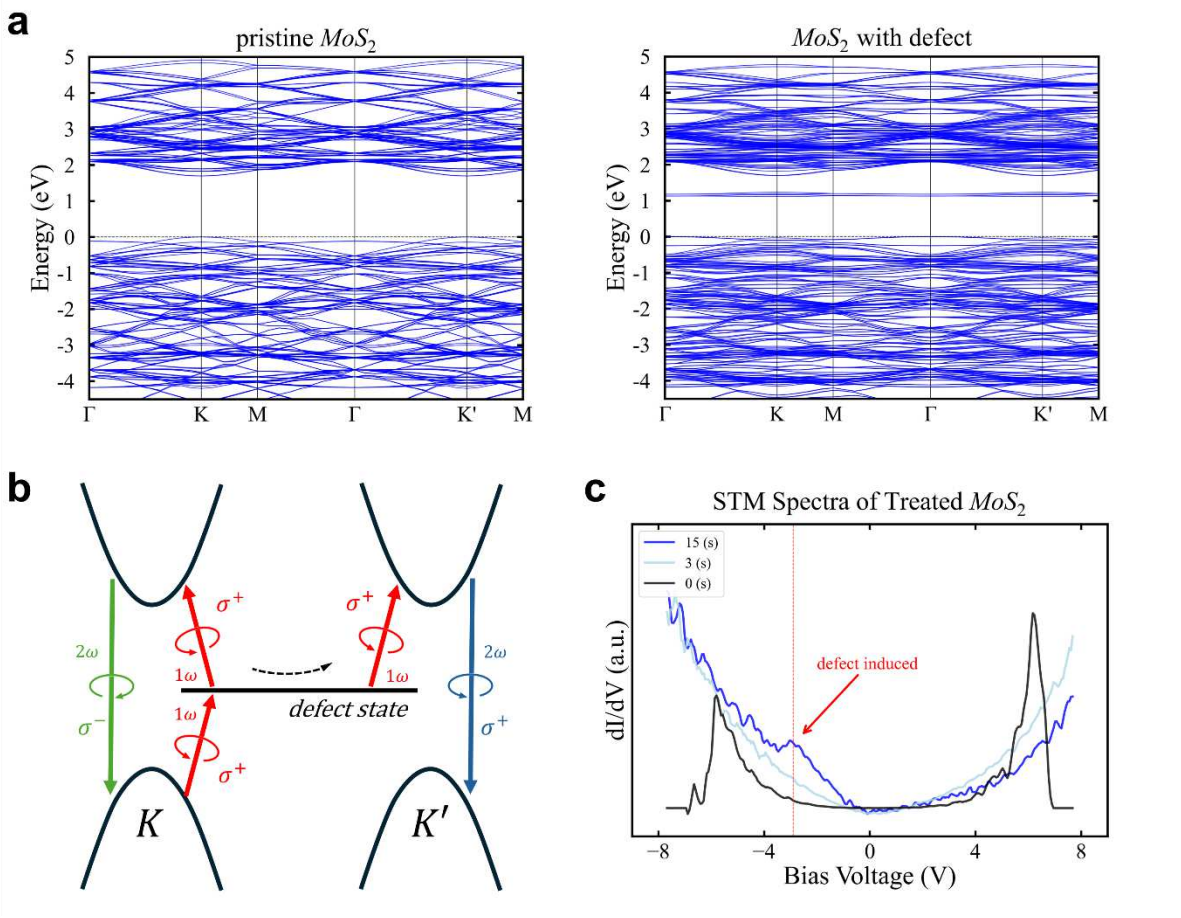


Figure 2. Defect-induced electronic states and their role in the HR-SHG enhancement of monolayer MoS_2. a, Band structure of MoS_2 with and without S-vacancy defects, where defect-induced states within the bandgap provide a resonant pathway for double excitation in the SHG process, thereby enhancing the overall SHG intensity. **b,** The illustration of valley-dependent optical selection rules at the K and K' points. In the presence of defect states, additional angular momentum compensation channels beyond the intrinsic threefold lattice symmetry become available, relaxing the valley-selective selection rules and enabling defect-assisted intervalley population transfer. **c,** STM-derived differential conductance spectra of monolayer MoS_2 subjected to Ar plasma treatment for 0, 3, 15 s. Compared with the pristine sample, the plasma-treated samples exhibit a progressive spectral evolution with increasing

treatment duration. In particular, after 15 s of plasma treatment, a defect-related spectral feature emerges, indicating the formation of defect-associated electronic states.

HR-SHG under Valley-Selective Excitation

Having established the electronic and chemical characteristics of the plasma-induced defects, we next examine how these defect states manifest in HR-SHG mapping. We performed HR-SHG measurements by illuminating the MoS_2 sample with σ^+ laser. The reflected SHG signal was collected using a reflection-mode microscopy system and subsequently passed through a quarter-wave plate followed by a rotatable linear analyzer for HR detection. Based on the calibrated analyzer-angle dependence, the SHG signals detected at analyzer angles of 45° and 225° were assigned to the left-handed circularly polarized (LCP) component, whereas those detected at 135° and 315° were assigned to the right-handed circularly polarized (RCP) component. This configuration enabled the two CP components to be separately resolved and mapped.

We first conducted HR-SHG mapping scans on MoS_2 samples subjected to different durations of Ar plasma treatment. Each mapping was acquired over a square region with a side length of 100 μm. The average pulse laser power was maintained at 60 mW, identical to that used for the linearly polarized SHG measurements described in Supplementary Information S.2. According to the valley-selective theory, monolayer MoS_2 exhibits different SHG intensities for LCP and RCP components under CP excitation due to valley selection rules. Figure 3a presents the SHG mapping results.

A clear contrast is observed between the LCP and RCP signals within each sample: the LCP signal is significantly stronger than the RCP signal, allowing extraction of the corresponding DOP for further quantitative analysis. The definition of DOP is given by:

$$DOP \equiv \frac{I_{\sigma-} - I_{\sigma+}}{I_{\sigma-} + I_{\sigma+}} \quad (1)$$

Notably, the mapping data also reveal the spatial uniformity. By examining spatial variations in the SHG intensity, we can infer local variations in defect density across a single MoS_2 flake. In low-dose plasma-treated samples, the RCP signals near the corners and edges are slightly stronger than those in the interior. This is attributed to the inherently weaker bonding environment of edge atoms, which renders them more susceptible to plasma-induced damage, resulting in locally elevated defect densities and hence stronger valley depolarization effects.[38]

As the Ar plasma bombardment time increases, the valley-polarized SHG signals become substantially stronger, indicating that the SHG response is highly sensitive to the increasing defect density. This enhancement originates from the formation of defect-induced intermediate energy states within the band structure, as discussed earlier. In pristine MoS_2, the SHG process requires

the simultaneous absorption of two photons to reach a virtual intermediate state. However, in the presence of defects, real intermediate states are introduced within the bandgap, allowing for a two-step resonant excitation pathway, as shown in figure 2b. This effectively enhances the second harmonic conversion efficiency, leading to a notable increase in overall SHG signal intensity.

To quantitatively model this process, we introduce a set of steady-state rate equations. The first equation describes generation and decay processes of excitons in the K valley:

$$\frac{dN_K}{dt} = g_{S\to K} - \frac{N_K}{\tau_{K\to S}} + G_{D\to K}N_D - \frac{N_k\left(N_{D,total} - N_D\right)}{\tau_{K\to D}} \tag{2}$$

where $g_{S\to K}$ is the pumping rate of laser source ; $G_{D\to K}$ is the second resonance coefficient from defect state to K point ; $N_{D,total}$ and N_D are the concentration of total and occupied defect state, respectively ; N_K is the concentration of exciton at K point ; $\tau_{K\to S}$ and $\tau_{K\to D}$ are the time constants of exciton recombination at K point and exciton transition from K to defect state, respectively.

The second equation describes similar processes in the K' valley:

$$\frac{dN_{K'}}{dt} = -\frac{N_{K'}}{\tau_{K'\to S}} + G_{D\to K'}N_D - \frac{N_{k'}\left(N_{D,total} - N_D\right)}{\tau_{K'\to D}} \tag{3}$$

where $G_{D\to K'}$ is the second resonance coefficient from the defect state to K' point ; $N_{K'}$ is the concentration of exciton at K' point ; $\tau_{K'\to S}$ and $\tau_{K'\to D}$ are the time constants of exciton recombination at K point and exciton transition from K' to defect state, respectively.

The third equation governs the formation and recombination at defect state:

$$\begin{aligned}\frac{dN_D}{dt} = &-(G_{D\to K} + G_{D\to K'})N_D + \frac{N_k\left(N_{D,total} - N_D\right)}{\tau_{K\to D}} \\ &+ \frac{N_{k'}\left(N_{D,total} - N_D\right)}{\tau_{K'\to D}} + \mathrm{G}_{S\to D} - \frac{N_D}{\tau_{D\to S}}\end{aligned} \tag{4}$$

where $\tau_{D\to S}$ is the time constants of exciton recombination at defect state.

By symmetry, we can presume $\tau_{K\to S} = \tau_{K'\to S}$, $G_{D\to K} = G_{D\to K'}$ and $\tau_{K\to S} = \tau_{K'\to S}$, apparently. Moreover, under intense pulsed laser excitation, a substantial population of photoexcited carriers can be captured at defect states, leading to carrier accumulation in these localized levels.[39,40] Such defect-occupied states are not necessarily inert. Instead, the accumulated carriers may undergo secondary optical excitation back into the K or K' valleys, thereby providing an additional channel for intervalley population redistribution and valley depolarization.[41] In this context, the approximation $N_{D,total} \approx N_D$ is justified under steady-state conditions. At steady-state equilibrium, the definition of valley polarization P_v yields:

$$P_v\left(N_{D,total}\right) = \frac{N_K - N_{K'}}{N_K + N_{K'}} = \frac{\mathrm{g_{S\to K}}}{\mathrm{g_{S\to K}} + 2\mathrm{G_{D\to K}}N_{D,total}} \approx 1 - \frac{2\mathrm{G_{D\to K}}}{\mathrm{g_{S\to K}}}N_{D,total} \tag{5}$$

It is clearly evident that as the defect density in the MoS_2 material increases, the value of $N_{D,total}$ correspondingly rises, thereby leading to valley depolarization in the HR-SHG signal.

To verify the DOP theory discussed earlier, we extracted azimuthal SHG profiles of the LCP and RCP components from each sample. Prior to calculating the DOP, the background signal was subtracted from both polarization components to minimize interference from background noise. Figure 3b and 3c illustrate the valley-polarized SHG intensity and the DOP results across various plasma treatment durations. As the plasma bombardment increases, a monotonic decrease in the DOP is observed, indicating progressive loss of valley coherence. Remarkably, the decline trend exhibits an approximately linear relationship, demonstrating the potential of this optical system to inspect the defect quantification in monolayer 2D material.

Moreover, under the same incident laser power, CP excitation produces a higher peak SHG intensity than linear excitation. For monolayer MoS_2, the D_{3h} symmetry of the second-order susceptibility predicts a twofold SHG-intensity enhancement under CP excitation for identical incident field amplitudes.[42,43] The complete derivation is provided in Supplementary Information S.4. This response indicates that HR-SHG can provide higher sensitivity than conventional linearly polarized SHG measurements.

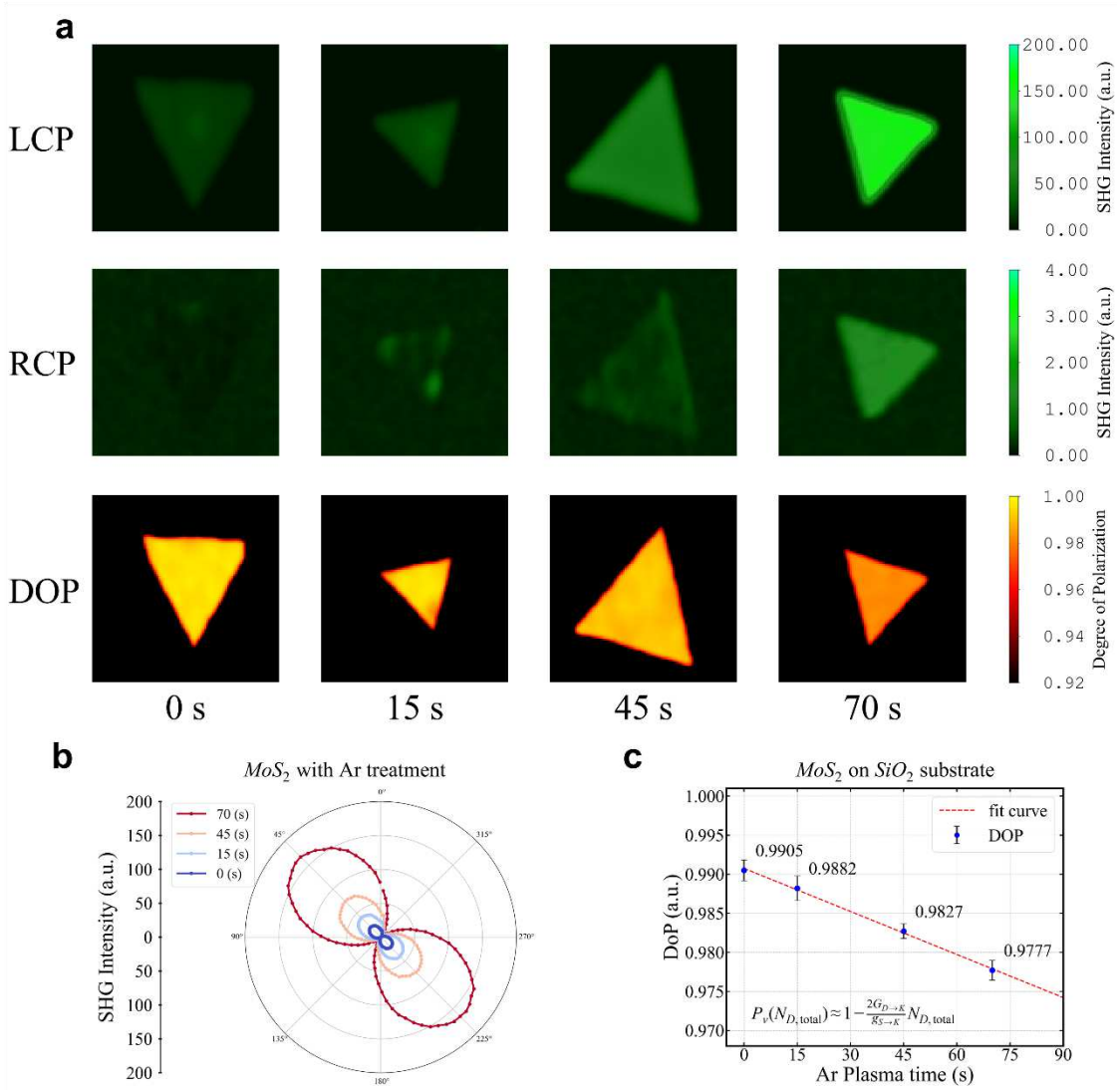


Figure 3. HR-SHG responses of monolayer MoS_2 with different defect densities. a, HR-SHG mapping of MoS_2 samples treated with Ar plasma bombardment for 0, 15, 45, and 70 s, respectively. Each mapping covers a square region with a side length of 100 μm. The excitation was performed using RCP light, and both LCP and RCP signals were collected, followed by the corresponding DOP analysis. **b,** Azimuthal HR-SHG patterns of MoS_2 samples subjected to Ar plasma bombardment. **c,** The corresponding DOP, which decreases progressively as the defect density increases, even though the SHG intensities of both HR components exhibit systematic enhancement.

High Sensitivity SHG under Circularly Polarized Excitation

Based on this enhanced sensitivity, we prepared MoS_2 samples with finer Ar plasma treatment intervals of 0, 3, 6, 9, 12, 15, 18 s to determine whether HR-SHG can distinguish finer defect variations. The average incident laser power was increased to 100 mW for this low-defect-density

series. As shown in figure 4a, the HR-SHG response varies distinctly with plasma treatment duration, indicating sensitivity not only to defect concentration but also to changes in defect configuration. Comparison with the XPS and KPFM results, which probe representative treatment durations, enables the continuous SHG evolution to be divided into three characteristic stages.

During Stage I (0–3 s), the SHG intensity increases rapidly immediately after plasma treatment. This behavior is consistent with the XPS results, which indicate preferential sulfur removal and the formation of isolated sulfur vacancies, as well as the KPFM measurements showing a reduction in work function associated with sulfur-vacancy-induced defect states. At this stage, energetic Ar ions primarily break Mo–S and residual surface S–S bonds, generating isolated sulfur vacancies and sulfur dangling bonds. These defects remain predominantly point defects while the long-range crystal symmetry is preserved, resulting in a pronounced enhancement of the SHG intensity.

During Stage II (3–9 s), the SHG intensity continues to increase but at a much slower rate. This suggests that plasma treatment mainly increases the concentration of existing point defects without significantly altering their local atomic configuration. In other words, the defect density continues to increase, whereas the defect type remains essentially unchanged. The weak variation in SHG therefore indicates that the nonlinear optical response depends not only on the number of defects but also on their local atomic configuration.

During Stage III (9–18 s), the SHG intensity increases approximately linearly with treatment duration, indicating a change in the dominant defect-evolution mechanism. Combined with the XPS and KPFM results, this behavior suggests that accumulated sulfur vacancies and dangling bonds progressively undergo reconstruction and oxidation. Reconstructed vacancies, sulfur-related species and oxidized defect complexes consequently become dominant. Once these chemically stabilized complexes are established, their concentration continues to increase while their local chemical character changes only slightly, producing the nearly linear SHG enhancement.

The agreement among SHG, XPS and KPFM obtained at representative treatment durations therefore reveals a transition from isolated sulfur-vacancy-related point defects to chemically stabilized reconstructed defect complexes in monolayer MoS_2.

Furthermore, previous reports have indicated that the defect density D_{it} of monolayer MoS_2 mechanically exfoliated (ME) from bulk crystals is significantly lower than that of CVD-grown samples, typically on the order of $\sim 10^{10}$ cm^{-2} compared to $\sim 10^{13}$ cm^{-2}.[44,45] To explore defect densities even lower than those of our pristine samples, we also prepared ME MoS_2 for measurement. As shown in figure 4b, under RCP excitation, the corresponding RCP signal component from ME sample was very close to the noise level almost undetectable at an excitation power of 100 mW, consistent with their much lower defect density relative to CVD-grown MoS_2. To overcome this limitation, we increased the excitation power based on the quadratic dependence

of SHG intensity on incident laser power. As the excitation power increased, HR-SHG responses became detectable and followed a square relationship with the intensity of the incident light, confirming the capability of our system to probe even ultralow-defect-density samples.

Finally, to verify the general applicability of our method beyond MoS_2, we also subjected monolayer WSe_2 samples to Ar plasma treatments of 0, 5, 10, 15, 20 s. As shown in figure 4c, under CP excitation, the WSe_2 samples exhibit a trend highly consistent with that observed in MoS_2, where the HR-SHG intensity increases systematically with plasma treatment duration, corresponding to increasing defect densities.These result demonstrates that the resolution of HR-SHG surpasses conventional optical characterization methods, establishing it as a highly sensitive and high-resolution tool for defect detection in two-dimensional materials. The HR-SHG response in WSe_2 also shows clear chiral selectivity and defect-induced enhancement behavior. The similar behavior observed in WSe_2 suggests that the method may be extendable to other monolayer transition-metal dichalcogenides.

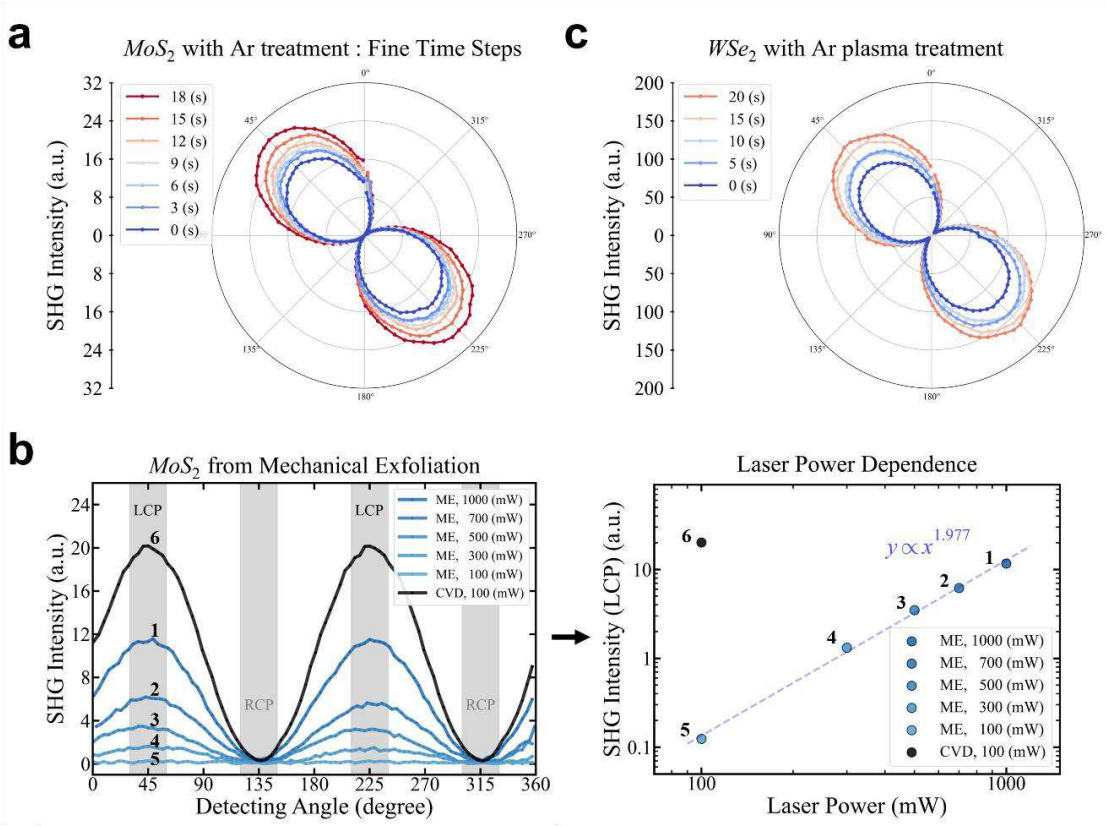


Figure 4. HR-SHG responses of plasma-treated MoS_2 and WSe_2 and mechanically exfoliated MoS_2. a, Azimuthal HR-SHG measurement of MoS_2 samples subjected to finely tuned Ar plasma treatment durations of 0, 3, 6, 9, 12, 15, 18 s. HR-SHG measurements of the samples reveal a clear increase in signal intensity with increasing treatment duration,

corresponding to higher defect densities. **b,** In addition, monolayer MoS_2 obtained by mechanical exfoliation (ME) was also examined. The corresponding laser-power dependence is shown on the right, confirming an approximately quadratic SHG response. By increasing the laser power, the same chiral-selective SHG response was observed, demonstrating the ultrahigh precision of our measurement technique. **c,** HR-SHG measurements of monolayer WSe_2 samples subjected to Ar plasma treatment (0, 5, 10, 15, 20 s). The SHG intensity exhibits a systematic increase with increasing treatment duration, indicating enhanced defect densities. The observed trend and chiral-selective response are highly consistent with those of MoS_2.

Conclusion

In this work, we establish HR-SHG as a quantitative optical approach for evaluating defects in monolayer MoS_2. By separately resolving the two CP components, the DOP serves as a direct indicator of defect-induced valley depolarization. Defect-associated electronic states introduce additional scattering and resonant pathways, thereby relaxing the intrinsic valley-selective optical rules, enhancing the SHG response and reducing the helicity contrast. The method distinguishes subtle defect variations, enables rapid large-area mapping and operates non-destructively at room temperature. These results highlight HR-SHG as a scalable platform for quantitative defect evaluation and quality monitoring in 2D semiconductors.

Methods

Synthesis of monolayer MoS_2

The monolayer MoS_2 single-crystal domains were synthesized via atmospheric-pressure chemical vapor deposition (APCVD). MoO_3 powder and sulfur powder were used as molybdenum and sulfur sources, respectively. During the growth process, sulfur powder was placed in the upstream region of the quartz tube outside the heating zone, while the MoO_3 powder and sapphire substrates were positioned in the center heating zone on a quartz boat. NaCl powder was mixed with the MoO_3 powder and placed toward the upstream side of the boat as a growth promoter. In addition, an inverted SiO_2/Si substrate was placed beneath the sapphire substrate to assist nucleation during growth.

Prior to deposition, all substrates were sequentially ultrasonically cleaned in acetone, ethanol, isopropanol (IPA), and deionized water for 5 minutes each. The quartz tube furnace was operated under atmospheric pressure with argon as the carrier gas at a flow rate of 60 sccm. The furnace temperature was ramped at a rate of 20 °C per minute. When the temperature reached 860 °C, the sulfur powder was moved closer to the heating zone to initiate sulfur evaporation. The temperature

was further increased to 890 °C and maintained for 3 minutes to grow monolayer MoS_2 single crystals. After the growth process, the heater was turned off and the furnace was allowed to cool naturally to room temperature before removing the samples.

The as-grown monolayer MoS_2 was transferred from the sapphire substrates to SiO_2/Si substrates using a wet transfer method. First, polymethyl methacrylate (PMMA) was spin-coated onto the MoS_2/sapphire substrate and baked at 100 °C for 10 minutes. The edges of the PMMA film were then scratched to allow solution penetration. The sample was subsequently immersed in a 1 M KOH solution at 110 °C for 2 minutes, followed by immersion in deionized water to separate the MoS_2/PMMA film from the sapphire substrate. The floating film was then transferred onto a SiO_2/Si substrate and left to dry at a tilted angle for more than 1 hour, followed by baking at 90 °C for 20 minutes to remove residual moisture. After transfer, the MoS_2 flakes were sequentially cleaned in acetone, isopropanol (IPA), and DI water, followed by immersion in N-methyl-2-pyrrolidone (NMP) at 110 °C for 20 min to remove residues. Then soaking the sample in acetone at 80 °C for at least 30 minutes, followed by rinsing with isopropanol at room temperature to remove acetone residues.

To introduce defects into the MoS_2 monolayers, argon plasma bombardment was performed using a capacitively coupled plasma (CCP) system. The chamber was evacuated to 2.5×10^{-2} Torr, after which argon gas was introduced at a flow rate of 12 sccm. When the chamber pressure stabilized at 9.5×10^{-2} Torr, a 5 W plasma was ignited. The treatment time was counted from the moment the plasma glow appeared. Different defect concentrations were achieved by varying the plasma treatment duration while keeping the plasma power constant.[46]

First-Principles Calculations

First-principles calculations were performed within the density functional theory framework using the CASTEP module implemented in Materials Studio. The exchange–correlation interaction was described using the generalized gradient approximation with the Perdew–Burke–Ernzerhof functional, together with norm-conserving pseudopotentials. Spin–orbit coupling was included throughout the geometry optimization and electronic-structure calculations. A 4 × 4 supercell of monolayer MoS_2 was constructed, and a vacuum layer of 20 Å was introduced along the out-of-plane direction to suppress interactions between periodic images. The plane-wave cutoff energy was set to 670 eV, and the Brillouin zone was sampled using a Monkhorst–Pack k-point grid generated with a reciprocal-space separation of 0.005 1/Å. The self-consistent-field energy tolerance was set to 1.0×10^{-6} eV per atom. Atomic positions were relaxed using the limited-memory Broyden–Fletcher–Goldfarb–Shanno algorithm while the lattice parameters were fixed. Geometry optimization was continued until the energy change, maximum residual force, maximum

stress, and maximum atomic displacement were below 1.0×10^{-5} eV per atom, 0.03 eV/Å, 0.05 GPa, and 0.001 Å, respectively. The sulfur-vacancy structure was constructed by removing one S atom from the 4 × 4 supercell, corresponding to one vacancy among 32 S lattice sites. Both the pristine and defective structures were fully relaxed using identical computational parameters. Their electronic band structures were subsequently calculated along the Γ–K–M–Γ–K′–M path.

Rotation Optical Axis Microscopy SHG System

Figure 5 illustrates the schematic diagram of the SHG measurement system. The light source used in this study is a femtosecond pulsed laser (central wavelength: 1030 nm; pulse width: 105 fs; repetition rate: 65 MHz). The laser beam first passes through an optical chopper operating at 1 kHz, allowing the lock-in amplifier to detect only signals referenced to this chopping frequency. In the excitation path, the beam passes through a set of polarization optics, including a half-wave plate (HWP) and a linear polarizer, to control both the laser intensity and the linear polarization. Subsequently, a combination of a HWP and a quarter-wave plate (QWP) is used to fine-tune and generate a high-precision circular polarization state (with ellipticity error less than 1%). The beam then passes through a rotatable polarizer to generate linearly polarized light with a controllable orientation.

Before entering the vacuum chamber, the beam is directed through two dichroic mirrors aligned parallel to the p- and s-polarization axes, respectively, to compensate for any phase shift introduced by the mirrors and thus preserve the polarization state.[47] An 800 nm long-pass filter is placed in front of the sample to block all visible light and any SHG signals generated upstream in the optical system, ensuring that only the fundamental beam reaches the sample surface.

On the detection side, a series of band-pass and short-pass filters are used to filter out the reflected SHG signals from the sample, allowing only the second-harmonic component centered at 515 nm to be transmitted. A QWP and a rotatable analyzer are used in conjunction with these filters to select specific SHG circularly polarized components. Based on the calibrated analyzer-angle response, signals measured at 45° and 225° were assigned to the LCP component, whereas those measured at 135° and 315° were assigned to the RCP component. The resulting 515 nm signal is detected and amplified by a photomultiplier tube (PMT), and the output is processed by the lock-in amplifier synchronized to the chopper frequency.

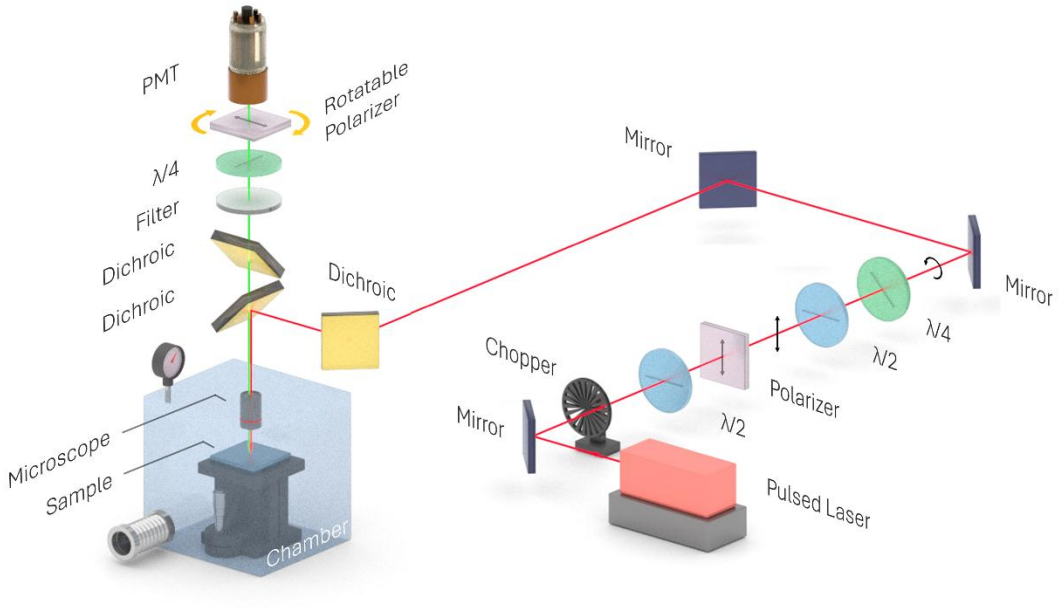


Figure 5. Schematic diagram of the experimental setup. The SHG measurement system consists of a femtosecond laser source, polarization-control optics, a vacuum chamber, and a detection system.

Acknowledgement

The authors would like to thank National Science and Technology Council, Taiwan for financially supporting this research under Contract No. NSTC 115-2112-M-006-006.

Reference

1 Chhowalla, M. *et al.* The chemistry of two-dimensional layered transition metal dichalcogenide nanosheets. *Nature chemistry* **5**, 263–275 (2013).

2 Mak, K. F., Lee, C., Hone, J., Shan, J. & Heinz, T. F. Atomically thin MoS 2: a new direct-gap semiconductor. *Physical review letters* **105**, 136805 (2010).

3 Huang, T.-E. *et al.* Quantitative Correlation for Recoverable Monolayer MoS2 Gas Sensing Mechanism: A Fundamental Approach. *The Journal of Physical Chemistry C* **127**, 18015–18025 (2023).

4 Ghatak, S., Pal, A. N. & Ghosh, A. Nature of electronic states in atomically thin MoS2 field-effect transistors. *ACS nano* **5**, 7707–7712 (2011).

5 Huang, T.-E. *et al.* The role of interface traps to affect monolayer MoS2 phototransistor. *Chinese Journal of Physics* **93**, 233–242 (2025).

6 Di Bartolomeo, A. *et al.* Hysteresis in the transfer characteristics of MoS2 transistors. *2D Materials* **5**, 015014 (2017).

7 Liu, D., Guo, Y., Fang, L. & Robertson, J. Sulfur vacancies in monolayer MoS2 and its electrical contacts. *Applied Physics Letters* **103** (2013).

8 Zhou, W. *et al.* Intrinsic structural defects in monolayer molybdenum disulfide. *Nano letters* **13**, 2615–2622 (2013).

9 Gali, S. M., Pershin, A., Lherbier, A., Charlier, J.-C. & Beljonne, D. Electronic and transport properties in defective MoS2: impact of sulfur vacancies. *The Journal of Physical Chemistry C* **124**, 15076–15084 (2020).

10 Santosh, K., Longo, R. C., Addou, R., Wallace, R. M. & Cho, K. Impact of intrinsic atomic defects on the electronic structure of MoS2 monolayers. *Nanotechnology* **25**, 375703 (2014).

11 Huang, T.-E. *et al.* Revealing the Active Role of the Gate Electrode in Weak-Light Detection. *ACS nano* **20**, 8266–8274 (2026).

12 Illarionov, Y. Y. *et al.* The role of charge trapping in MoS2/SiO2 and MoS2/hBN field-effect transistors. *2D Materials* **3**, 035004 (2016).

13 Fang, N., Nagashio, K. & Toriumi, A. Experimental detection of active defects in few layers MoS2 through random telegraphic signals analysis observed in its FET characteristics. *2D Materials* **4**, 015035 (2016).

14 Gelczuk, Ł. *et al.* Probing Defects in MoS2 Van der Waals Crystal through Deep-Level Transient Spectroscopy. *physica status solidi (RRL)–Rapid Research Letters* **14**, 2000381 (2020).

15 Sun, S. *et al.* Defect-rich monolayer MoS2 as a universally enhanced substrate for surface-enhanced Raman scattering. *Nanomaterials* **12**, 896 (2022).

16 Dong, H. *et al.* Fluorescent MoS2 quantum dots: ultrasonic preparation, up-conversion and down-conversion bioimaging, and photodynamic therapy. *ACS applied materials & interfaces* **8**, 3107–3114 (2016).

17 Vancsó, P. *et al.* The intrinsic defect structure of exfoliated MoS2 single layers revealed by Scanning Tunneling Microscopy. *Scientific reports* **6**, 29726 (2016).

18 Huang, W., Xiao, Y., Xia, F., Chen, X. & Zhai, T. Second harmonic generation control in 2D layered materials: status and outlook. *Advanced Functional Materials* **34**, 2310726 (2024).

19 Hardhienata, H., Prylepa, A., Stifter, D. & Hingerl, K. in *Journal of Physics: Conference Series.* 012046 (IOP Publishing).

20 Li, Y. *et al.* Probing symmetry properties of few-layer MoS2 and h-BN by optical second-harmonic generation. *Nano letters* **13**, 3329–3333 (2013).

21 Zeng, X. *et al.* Nonlinear optics of two-dimensional heterostructures. *Frontiers of Physics* **19**, 33301 (2024).

22 Chow, P. K. *et al.* Defect-induced photoluminescence in monolayer semiconducting transition metal dichalcogenides. *ACS nano* **9**, 1520–1527 (2015).
23 Akkanen, S. T. M. *et al.* Enhanced Nonlinear Optical Responses in MoS2 via Femtosecond Laser-Induced Defect-Engineering. *Advanced Functional Materials* **34**, 2406942 (2024).
24 Zeng, H., Dai, J., Yao, W., Xiao, D. & Cui, X. Valley polarization in MoS2 monolayers by optical pumping. *Nature nanotechnology* **7**, 490–493 (2012).
25 Mujeeb, F., Chakrabarti, P., Mahamiya, V., Shukla, A. & Dhar, S. Influence of defects on the valley polarization properties of monolayer MoS 2 grown by chemical vapor deposition. *Physical Review B* **107**, 115429 (2023).
26 Kioseoglou, G. *et al.* Valley polarization and intervalley scattering in monolayer MoS2. *Applied Physics Letters* **101** (2012).
27 Ho, Y. W. *et al.* Measuring valley polarization in two-dimensional materials with second-harmonic spectroscopy. *ACS Photonics* **7**, 925–931 (2020).
28 Mennel, L., Paur, M. & Mueller, T. Second harmonic generation in strained transition metal dichalcogenide monolayers: MoS2, MoSe2, WS2, and WSe2. *APL Photonics* **4** (2019).
29 Mouchliadis, L. *et al.* Probing valley population imbalance in transition metal dichalcogenides via temperature-dependent second harmonic generation imaging. *npj 2D Materials and Applications* **5**, 6 (2021).
30 Pacilè, D. *et al.* Narrowing of d bands of FeCo layers intercalated under graphene. *Applied Physics Letters* **118** (2021).
31 Giannozzi, P. *et al.* QUANTUM ESPRESSO: a modular and open-source software project for quantumsimulations of materials. *Journal of physics: Condensed matter* **21**, 395502 (2009).
32 Giannozzi, P. *et al.* Advanced capabilities for materials modelling with Quantum ESPRESSO. *Journal of physics: Condensed matter* **29**, 465901 (2017).
33 Zhu, B., Lang, J. & Hu, Y. H. S-Vacancy induced indirect-to-direct band gap transition in multilayer MoS2. *Physical Chemistry Chemical Physics* **22**, 26005–26014 (2020).
34 Feng, L.-p., Su, J. & Liu, Z.-t. Effect of vacancies on structural, electronic and optical properties of monolayer MoS2: a first-principles study. *Journal of Alloys and Compounds* **613**, 122–127 (2014).
35 Zhang, X. *et al.* Unravelling the effect of sulfur vacancies on the electronic structure of the MoS2 crystal. *Physical Chemistry Chemical Physics* **22**, 21776–21783 (2020).
36 Ataca, C. & Ciraci, S. Functionalization of single-layer MoS2 honeycomb structures. *The Journal of Physical Chemistry C* **115**, 13303–13311 (2011).
37 Guo, Y., Liu, D. & Robertson, J. Chalcogen vacancies in monolayer transition metal dichalcogenides and Fermi level pinning at contacts. *Applied Physics Letters* **106** (2015).
38 Spirko, J. A., Neiman, M. L., Oelker, A. M. & Klier, K. Electronic structure and reactivity of

defect MoS2: I. Relative stabilities of clusters and edges, and electronic surface states. *Surface science* **542**, 192–204 (2003).

39 Yen, T.-Y. *et al.* Correlation of time-dependent nonlinear response with phosphorus concentration in Si ultrathin film. *Surfaces and Interfaces* **36**, 102541 (2023).

40 Chen, W.-T., Yen, T.-Y., Hung, Y.-H. & Lo, K.-Y. Structure of an in situ phosphorus-doped silicon ultrathin film analyzed using second harmonic generation and simplified bond-hyperpolarizability model. *Nanomaterials* **12**, 4307 (2022).

41 Yen, T.-Y., Shih, M.-T., Song, L.-F., Hung, K.-M. & Lo, K.-Y. Unveiling dopant concentration in boron doped Si ultrathin film: Enhanced analysis using time-dependent second harmonic generation. *Surfaces and Interfaces* **41**, 103236 (2023).

42 Shree, S. *et al.* Interlayer exciton mediated second harmonic generation in bilayer MoS2. *Nature Communications* **12**, 6894 (2021).

43 Clark, D. *et al.* Strong optical nonlinearity of CVD-grown MoS 2 monolayer as probed by wavelength-dependent second-harmonic generation. *Physical Review B* **90**, 121409 (2014).

44 Liu, H., Wong, S. L. & Chi, D. CVD growth of MoS2-based two-dimensional materials. *Chemical Vapor Deposition* **21**, 241–259 (2015).

45 Addou, R., Colombo, L. & Wallace, R. M. Surface defects on natural MoS2. *ACS applied materials & interfaces* **7**, 11921–11929 (2015).

46 Chen, P.-C. *et al.* Effective N-methyl-2-pyrrolidone wet cleaning for fabricating high-performance monolayer MoS2 transistors. *Nano Research* **12**, 303–308 (2019).

47 Harter, J., Niu, L., Woss, A. & Hsieh, D. High-speed measurement of rotational anisotropy nonlinear optical harmonic generation using position-sensitive detection. *Optics letters* **40**, 4671–4674 (2015).

Supplementary Files

This is a list of supplementary files associated with this preprint. Click to download.

- SupplementaryInformation.docx